Comparative study of photoelectron momentum distributions from Kr and CO_2 near a backward rescattering caustic by carrier-envelope-phase mapping

Tomoya Mizuno [1,*] Tianqi Yang,[1] Takayuki Kurihara [1] Nobuhisa Ishii [1,†] Teruto Kanai,[1]
Oleg I. Tolstikhin [2] Toru Morishita,[3] and Jiro Itatani [1]

[1]*The Institute for Solid State Physics, The University of Tokyo, 5-1-5 Kashiwanoha, Kashiwa, Chiba 277-8581, Japan*
[2]*Moscow Institute of Physics and Technology, Dolgoprudny 141700, Russia*
[3]*Institute for Advanced Science, The University of Electro-Communications, 1-5-1 Chofu-ga-oka, Chofu-shi, Tokyo 182-8585, Japan*

We study carrier-envelope-phase- (CEP-) dependent photoelectron momentum distributions (PEMDs) of Kr atoms and randomly oriented CO_2 molecules exposed to sub-two-cycle intense infrared fields with linear polarization. The adiabatic theory predicts that, at fixed laser parameters (intensity, pulse duration, and CEP), the PEMDs for targets with equal ionization potentials considered across a backward rescattering caustic have identical shapes and only their absolute values depend on the target. We choose Kr and CO_2 as targets with almost identical ionization potentials (approximately 14 eV) to explore this behavior of PEMDs. We find that the measured PEMDs for Kr and CO_2 have cutoff structures, which are associated with the caustics, with identical decaying profiles. We also reveal that CEP-dependent PEMDs around the cutoff exhibit target dependence, reflecting the differences in the differential cross sections (DCSs) of elastic rescattering and tunneling ionization rates. Furthermore, we extract the DCSs from the measured PEMDs around the cutoffs at different CEPs based on the adiabatic theory. The extracted DCSs agree with ones calculated by using the single-active-electron (SAE) scattering model, which includes all multiple-scattering processes, with orientation averaging for CO_2. In contrast, the independent-atom model, which only considers single-scattering processes, cannot reproduce the extracted DCSs of CO_2 at low scattering momenta. This finding indicates that multiple scattering is not negligible in the momentum range of 1.5–2.5 a.u. The extracted DCSs also show interference features assigned to multicenter scattering of O-O and C-O. These results confirm that the signature of electron interference is retained after orientation averaging, indicating that the internuclear distances of the constituent atoms can be retrieved from the CEP-dependent PEMDs for randomly oriented molecules using the SAE model.

I. INTRODUCTION

Strong-field ionization is a fundamental process in atomic and molecular physics and has various applications in attosecond science. According to the three-step model [1,2], an electron wave packet produced by the tunnel ionization of an atom or molecule is accelerated by an optical field and subsequently recollides with the parent ion. This recollision leads to recombination or electron rescattering. Recombination induces the emission of high-energy photons or high-order harmonic generation (HHG), whereas elastic rescattering in the presence of strong optical fields induces the emission of high-energy photoelectrons, which contain information about elastic electron-ion scattering [3]. The cutoff structure of a photoelectron momentum distribution (PEMD) was investigated by a classical model [4]. Furthermore, it was reported that in the vicinity of a backward rescattering cutoff, a PEMD can be factorized into a differential cross section (DCS) for elastic electron-ion scattering and a returning photoelectron wave packet [5–13], thereby allowing the extraction of DCS from the PEMD [14–30].

In the adiabatic theory [10,13], the cutoff of PEMDs can be further elaborated using the concept of caustics; caustics are defined by the degenerated singularity of the action described by the Hamiltonian formulation [31–37]. The adiabatic theory introduces a quantum caustic that is derived from the classical action as well as another quantum term stemming from the evolution of the Siegert state describing ionization by the field. It has been shown that a sliced PEMD in a direction normal to the caustics exhibits the characteristic shape described by the Airy function. The PEMD beyond the quantum caustic exhibits exponential decay because the argument of the Airy function becomes zero at its location [13]. A PEMD contains several caustics, corresponding to each half cycle in the laser pulses. Every half cycle, the electric field produces one backward rescattering half cycle cutoff (HCO) in the PEMD. Then each caustic corresponds to one specific HCO. Therefore, the quantum caustic can be used to define the exact position of the HCO. The factorization formula based on the adiabatic theory holds in the limited region around the caustic [13]. It predicts that the shape of the PEMD around the caustic is completely determined by the laser pulse, regardless of the

---

*mizuno.tomoya@issp.u-tokyo.ac.jp
†Present address: Kansai Photon Science Institute, National Institutes for Quantum Science and Technology (QST), 8-1-7 Umemidai Kizugawa, Kyoto 619-0215, Japan.

target species, whereas the position of the caustic depends on the laser pulse and targets. This is the theoretical basis of the carrier-envelope-phase (CEP) mapping to determine the DCSs from the measured PEMDs around the caustics [29].

Experimentally, errors in the DCSs extracted from measured PEMDs arise because of two factors. First, the typical multicycle laser pulses contain several half cycles with the same field direction and nearly identical field strengths, causing overlapping of the HCOs in the PEMD. In this study we use sub-two-cycle pulses to extract the HCOs at the highest and second-highest momenta, resolving the rescattering events at different times and excluding the ambiguity of the field amplitude associated with multicycle pulses. In addition, we can control the positions of the HCOs by varying the CEP; this corresponds to changing the momentum at the instance of rescattering [24]. Second, the measured PEMDs originate from different positions within the focal volume. Generally, the intensity of a laser beam is not spatially uniform; thus, the measured PEMDs reflect the atomic responses at different intensities. However, we experimentally confirm that CEP-dependent PEMDs around the HCOs for Xe atoms are reproduced by the factorization formula based on the adiabatic theory at a single laser intensity, resulting in the successful extraction of the elastic scattering DCSs [29]. We also find that measured PEMDs in the plateau region are remarkably influenced by the focal volume effects. Thus we conclude that only the decay profile of the measured PEMDs beyond the caustics can be analyzed using the factorization formula without considering the volume effects.

The DCS extraction of rare-gas atoms is well established and the atomic DCSs reflect the effective one-center atomic potentials [20,38]. However, molecular DCSs are more complicated because of their multicenter potentials [18,39]. Molecular DCSs, in particular, their dependence on the scattering angle, are extracted from angle-resolved PEMDs around the cutoffs [19,26,28,40]. The extraction of DCSs that depend on the scattering momentum has not been established yet because in most of the previous experiments, PEMDs in the plateau regions [18,41–44] were used; in these regions, the PEMDs are heavily influenced by the focal volume effects [29], resulting in difficulties in accurately extracting the DCSs. Another approach to extracting momentum-dependent DCSs is to measure PEMDs at different laser intensities [21,22]. However, this approach also leads to inaccurate extraction because of the volume effect. It is technically difficult to control laser intensity without changing other conditions. To solve this problem, we control the CEP of few-cycle laser pulses to change the rescattering momentum effectively while maintaining the same focusing conditions [24], thereby enabling us to accurately extract the molecular DCSs.

In this study we investigate the HCO structure of PEMDs produced by ionizing Kr atoms and randomly oriented CO_2 molecules with linearly polarized two-cycle infrared pulses. At fixed laser parameters, the measured PEMDs of Kr and CO_2 have similar distributions around the caustic. This means that the argument of the Airy function describing the shape of a PEMD around the caustic is independent of the targets, while the absolute electron yields and their CEP dependence are different, reflecting the target dependence of the DCSs and tunneling ionization rates. We find that

the CEP-dependent PEMDs of Kr and CO_2 can be quantitatively reproduced by the adiabatic theory. Furthermore, the extracted DCSs of CO_2 agree with the calculated DCSs within the single-active-electron (SAE) approximation, including all multiple-scattering contributions. In contrast, the independent-atom model (IAM), which considers only the single-scattering contribution, is inaccurate. The quantitative agreement between the extracted DCSs and the SAE calculations indicates that the structures in the orientation-dependent DCSs arise because of electron interference during multicenter scattering by molecules. In addition, the large discrepancy between the SAE and the IAM calculations indicates that the multiple scattering contributes remarkably to backward elastic scattering in the low-scattering-momentum range of 1.5–2.5 a.u.

The paper is organized as follows. In Sec. II we present a factorization formula in the adiabatic theory. This formula describes PEMDs near backward rescattering caustics [13]. In Sec. III we outline the experimental setup and procedures to analyze the measured PEMDs [24,29]. In Sec. IV we compare the experimental and theoretical results and discuss the roles of multicenter and multiple scattering. Section V summarizes this study.

II. ADIABATIC THEORY FOR RESCATTERING PROCESSES AROUND THE CAUSTIC

In this section the structure of strong-field PEMDs near a backward rescattering caustic is analyzed using the factorization formula derived in Ref. [13] within the adiabatic theory [10]. We briefly introduce the theoretical framework for atomic and molecular targets. Further, we show that the PEMDs in the polarization direction around caustics have a universal shape that can be described by the Airy function due to the degenerate singularity [31–37]. We also present how the CEP dependence of the photoelectron yields around the caustic depends on the targets and this target dependence can be employed to extract scattering momentum-dependent DCSs [24,29].

A. Basic parameters of a laser field

We assume that the ionizing laser field is linearly polarized along the laboratory z axis, i.e., $\mathbf{F}(t) = F(t)\mathbf{e}_z$. To model the experimental results, we set

$$F(t) = F_0 \exp[-(\sqrt{2\ln 2}\,t/T)^2]\cos(\omega t - \phi). \quad (1)$$

Here we assume a Gaussian envelope, in which the laser field is characterized by its amplitude F_0, duration (full width at half maximum of intensity) T, carrier frequency ω, and CEP ϕ. In the present experiment, we use 1600-nm pulses with typical amplitude $F_0 \sim 0.0492$ a.u. (intensity $I = cF_0^2/8\pi \sim 8.5 \times 10^{13}$ W/cm^2, where c is the speed of light), duration $T \sim 14$ fs, and CEP ϕ varied continuously.

The photoelectron momentum is defined as $\mathbf{k} = (k_\perp, k_z)$. Photoelectron momentum distributions for atoms and randomly oriented molecules for linearly polarized pulses are axially symmetric about k_z. In our experiment, only the one-dimensional cut of a PEMD along the polarization direction $P(k_z)$ is measured. In the vicinity of a caustic, the function

$P(k_z)$ is determined by the photoelectrons that rescattered exactly in the backward direction. Therefore, we present the rescattering amplitude for this particular case only; the general case of rescattering at an arbitrary angle is treated in Ref. [13].

B. Siegert state of Kr and CO_2 for static fields

In the adiabatic regime, strong-field ionization proceeds as if the ionizing field were static and equal to the instantaneous laser field [10]. The unperturbed initial state of a target in the presence of a static electric field $\mathbf{F} = F\mathbf{e}_z$ turns into the corresponding Siegert state [45]. Then all ionization observables can be described in terms of the properties of the Siegert state. We need the complex Siegert eigenvalue $E(F) = \mathcal{E}(F) - \frac{i}{2}\Gamma(F)$ that defines the Stark-shifted energy $\mathcal{E}(F)$ and ionization rate $\Gamma(F)$ of the state and the amplitude $A(k_\perp; F)$ of the transverse momentum distribution (TMD) of outgoing electrons in the asymptotic part of a Siegert eigenfunction. We define the TMD amplitude as $A_0(F) = A(k_\perp = 0; F)$. The field-free energy of the initial state is $E_0 = E(0)$. Only electrons that tunnel with zero transverse momentum return for rescattering; thus we set $k_\perp = 0$. By substituting $F \to F(t)$, we obtain the instantaneous properties of the Siegert state that characterizes the target.

To explore the structure of PEMDs, we choose Kr and CO_2 as the target media, whose binding energies E_0 are almost the same (approximately 14 eV). As will be shown, the shapes and locations of the PEMDs around the caustics for those targets for the same pulses are nearly identical. The orientation of CO_2 is described by the Euler angles (α, β, γ) defining a rotation from the laboratory frame to the molecular frame. Here β is defined as the angle between the polarization vector $\mathbf{e}_z$ and molecular axis; α determines the rotation of the molecular axis relative to the polarization axis; γ is set to zero.

We calculate the corresponding Siegert states within the SAE approximation, where the potential parameters are adjusted to obtain their binding energies. For Kr we numerically solve the time-independent Schrödinger equation in the same manner as in Ref. [13] using the method proposed in Ref. [45]. For CO_2, we describe the Siegert state using the leading-order approximation of the weak-field asymptotic theory (WFAT) [46], using the model potential described in Ref. [28]. In this approximation, the Siegert energy is given by the first-order perturbation theory. Thus, the β-dependent Siegert energy $E_\beta(F(t))$ of CO_2 is approximated by the binding energy E_0 of the unperturbed highest occupied molecular orbital (HOMO) because of the absence of linear Stark shift in the case of nonpolar molecules. In the WFAT [46,47], the β-dependent ionization rate $\Gamma_\beta(F(t))$ and the TMD amplitude $A_{0\beta}(F(t))$ for CO_2 are given by

$$\Gamma_\beta(F(t)) = \left(|G_{00}(\beta)|^2 + \frac{F}{2\varkappa^2}|G_{01}(\beta)|^2\right)W_{00}(F) \qquad (2)$$

and

$$|A_{0\beta}(F(t))|^2 = \frac{4\pi\varkappa}{F}|G_{00}(\beta)|^2 W_{00}(F), \qquad (3)$$

where $F = |F(t)|$, $\varkappa = \sqrt{-2E_0}$, $G_{00}(\beta)$ and $G_{01}(\beta)$ denote the structure factors for the dominant and next-to-dominant ionization channels, respectively, defined in terms
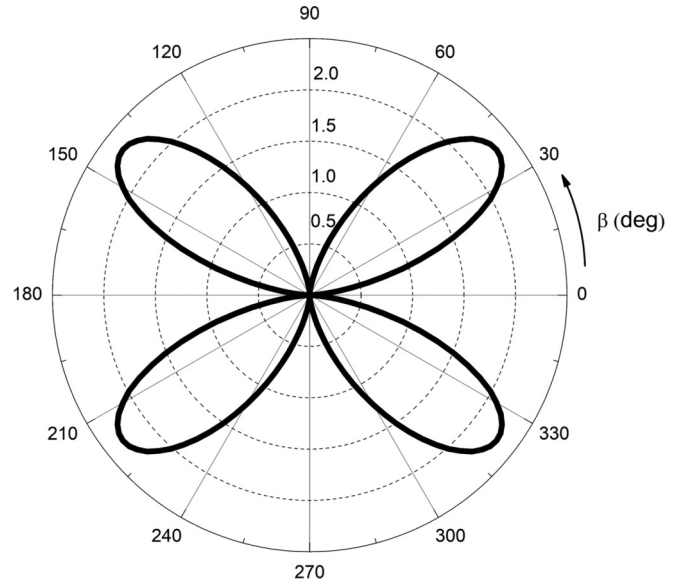

FIG. 1. Calculated squared structure factor $|G_{00}(\beta)|^2$ of CO_2.

of the unperturbed ionizing orbital, and W_{00} denotes the field factor, whose explicit form is written as

$$W_{00}(F) = \frac{\varkappa}{2}\left(\frac{4\varkappa^2}{F}\right)^{2/\varkappa-1}\exp\left(-\frac{2\varkappa^3}{3F}\right). \qquad (4)$$

Equation (3) shows the analytical representation of the TMD within the WFAT [46,47], where its field dependence is given by the term W_{00}/F. Moreover, the molecular orientation dependence of the TMD amplitude is characterized by the structure factor of $G_{00}(\beta)$. The squared structure factor $|G_{00}(\beta)|^2$ of CO_2 is shown in Fig. 1, where the cloverlike structure reflects the π_g orbital of the HOMO.

C. Elastic scattering amplitude

An electron released from a target atom by tunneling may return to the parent ion within one optical cycle and undergo elastic rescattering. A rescattering event is characterized by spherical scattering angles $\Omega = (\theta, \varphi)$ measured relative to the direction of the incident momentum. The rescattering event for an atomic target is described by the scattering amplitude $f(k, \theta)$ defining the DCS $d\sigma/d\Omega = |f(k, \theta)|^2$, where $k > 0$ is the incident momentum and θ is the scattering angle [48]. For a molecule, the scattering amplitude $f_\beta(k, \Omega)$ defines the DCS $d\sigma_\beta/d\Omega = |f_\beta(k, \Omega)|^2$ at the fixed-space molecule characterized by $\alpha = 0$ and β. Herein we consider only the backward rescattering event, corresponding to $\theta = \pi$. Accordingly, the DCSs are obtained using the same SAE potentials for the Siegert state calculations for both Kr and CO_2.

D. Classical and quantum caustics in the backward rescattering process

After rescattering, the electron flies away with asymptotic momentum $\mathbf{k}$. In the general case, each half cycle of the laser field $F(t)$ produces a pair of long and short classical rescattering trajectories contributing to the PEMD at the same final

k in a certain region of the photoelectron momentum space. The two trajectories coalesce at the high-energy boundary of the region, which is called the classical caustic generated by the given half cycle. From the singularity perspective, the classical caustic is a surface on which the saddle-point equation of the classical action has a doubly degenerate root. The two classical trajectories contribute to the PEMD on the lower-energy side of the caustic and none on the higher-energy side. The caustic is a surface of revolution about the k_z axis. Let k_c denote the point at which it crosses the k_z axis. Let t_i and t_r be the moments of ionization and rescattering, respectively, and $\mathbf{u}_f = u_f \mathbf{e}_z$ be the incident momentum of rescattering for coalesced trajectories contributing to the PEMD $P(k_z)$ at $k_z = k_c$. The values of k_c, t_i, t_r, and u_f are completely determined based on classical mechanics and laser field $F(t)$. The explicit equations defining these kinematic characteristics of rescattering are given in Ref. [13].

In the present experiment, we measure the PEMDs $P(k_z)$ only at $k_z > 0$. So we are interested in only positive caustics $k_c > 0$ with a negative momentum of rescattering $u_f < 0$ generated by negative half cycles of the pulse $F(t) < 0$. As ϕ varies, the half cycle shifts to the left ($\phi < 0$) or right ($\phi > 0$) along the time axis and the value of k_c changes continuously. In addition to the outermost caustics, there are inner caustics generated by half cycles with different amplitudes. Note that the set of *all* caustics generated by the pulse defined in Eq. (1) is transformed into itself as ϕ varies by 2π while the other pulse parameters are kept fixed, but each individual caustic is generally not a periodic function of ϕ (see Ref. [29]).

Next we discuss the corresponding quantum caustic. According to the adiabatic theory, the time integral defining the PEMD, which is presented later, in the vicinity of a given classical caustic has two saddle points associated with the long and short rescattering trajectories [13]. However, in addition to the classical term, describing propagation along the trajectories, the action $S_r(t; k_z)$ in the integrand contains a quantum term $-\int^t E(F(t'))dt'$ that accounts for the evolution of the ionizing Siegert state [10]. The surface in the photoelectron momentum space where the two saddle points of the action $S_r(t; k_z)$ including this term coalesce is called the quantum caustic, which is assigned to the A_2 singularity due to the degeneracy of $n = 2$. The action $S_r(t; k_z)$ was Taylor expanded up to the third order around the moment of rescattering t_r at the caustic, as described in Ref. [13]. We expand the action in the third-order Taylor series around $\tilde{t}_r = t_r - S_r''(t_r; k_z)/S_r'''$, instead of t_r, at the backward rescattering of $\theta = \pi$, expressed as

$$S_r(t; k_z) \simeq S_r(\tilde{t}_r; k_z) + |u_f|(k_z - k_q)(t - \tilde{t}_r) + \frac{S_r'''}{6}(t - \tilde{t}_r)^3, \tag{5}$$

where k_q represents the quantum caustic corresponding to $\theta = \pi$ and S_r''' represents the third-order derivative of the classical action at t_r and independent of k_z. The prime denotes the derivative with respect to time t. Indeed, Eq. (5) is the normal form of the A_2 singularity [34,35]. (The normal form is given in Appendix A.) Thus, the action $S_r(t; k_z)$ has the doubly degenerate singular point that is $\tilde{t}_r$ at the quantum caustic.

The quantum caustic is shifted with respect to the classical caustic toward higher energies; its position for an arbitrary

scattering angle θ is defined in Ref. [13]. The quantum caustic is also a surface of revolution about the k_z axis. As defined, k_q denotes the point at which it crosses the k_z axis, corresponding to $\theta = \pi$. The value of k_q is related to k_c as

$$k_q = k_c + q, \tag{6}$$

where the quantum shift q is given by

$$q = \frac{-E(F(t_i))}{(t_r - t_i)|F(t_i)|}. \tag{7}$$

Notably, the shift depends on the pulse (defining t_i and t_r) as well as the target. Furthermore, the shift is generally complex because the Siegert eigenvalue $E(F)$ is complex. However, for the present targets and pulses, the imaginary part of k_q is small and, for simplicity, we disregard it in the current discussion. Then the shift is defined by the instantaneous value of the Stark-shifted energy $\mathcal{E}(F(t_i))$ of the initial state at the moment of ionization. In the case of an adequately small Stark shift, $E(F(t_i)) \sim E_0$ and q can be approximately given by

$$q \simeq \frac{-E_0}{(t_r - t_i)|F(t_i)|}, \tag{8}$$

wherein the theory predicts that q is target dependent only via the value of the energy E_0. Therefore, at any orientation angle, Kr and CO_2 would exhibit the same value of q for the same laser pulses.

E. Universality of the PEMD around a caustic

We present the rescattering amplitude based on the adiabatic theory, as detailed in Ref. [13]. First, we explain the case of an atomic target; that of a molecular target is discussed later. The amplitude from a given half cycle in the vicinity of the corresponding classical and quantum caustics can be expressed as

$$I(k_z) = \int_{-\infty}^{\infty} \frac{A_0(F(t_i))f(|u_f|, \pi)}{|(t - t_i)^3 F(t_i)|^{1/2}} \exp[iS_r(t; k_z)]dt. \tag{9}$$

As discussed earlier, the action $S_r(t; k_z)$ contains a quantum caustic associated with the A_2 singularity. Substituting the expansion in Eq. (5) into Eq. (9) and performing integration using the steepest-decent method, the rescattering amplitude of the photoelectron around a quantum caustic can be approximately given by

$$\begin{aligned} I(k_z) &\simeq \mathrm{Ai}[C(k_z - k_q)] \\ &\times \left(\frac{2}{S_r'''}\right)^{1/3} \frac{2\pi A_0(F(t_i))f(|u_f|, \pi)}{|(t_r - t_i)^3 F(t_i)|^{1/2}} \\ &\times \exp[iS_r(\tilde{t}_r, k_z)], \end{aligned} \tag{10}$$

where $\mathrm{Ai}(z)$ represents the Airy function. The coefficient C is given by

$$C = \left(\frac{2}{S_r'''}\right)^{1/3} |u_f|. \tag{11}$$

Moreover, the PEMD $P_c(k_z)$ around a caustic can be obtained as $P_c(k_z) = |I(k_z)|^2$, given by the factorization formula used for extracting the DCS $|f(|u_f|, \pi)|^2$ as

$$P_c(k_z) = |f(|u_f|, \pi)|^2 W(k_z), \tag{12}$$

where $W(k_z)$ represents the returning electron wave packet (RWP) around the caustic for an atom (and a fixed-space molecule), defined in Ref. [13] as

$$W(k_z) = |\text{Ai}[C(k_z - k_q)]|^2 \left| \frac{2}{S_r'''} \right|^{2/3} \frac{4\pi^2 |A_0(F(t_i))|^2}{(t_r - t_i)^3 |F(t_i)|}$$

$$\times \exp\left(-\int_{-\infty}^{t_i} \Gamma(F(t))dt\right). \quad (13)$$

Note that the Airy function $\text{Ai}(z)$ represents the universal distribution for various phenomena associated with the A_2 singularity class of a caustic [31–33,36,37], as detailed in Appendix A. The Airy function in $W(k_z)$ describes the dependence of $P_c(k_z)$ on k_z. All other factors in $P_c(k_z)$ do not depend on k_z and they merely influence the absolute yield. The argument of the Airy function becomes zero at the quantum caustic $k_z = k_q$, beyond which $P_c(k_z)$ decays rapidly. The quantum caustic quantitatively specifies the meaning of a vague experimental concept of the HCO. As the coefficient C is determined only by the laser pulse, the shape of $P_c(k_z)$ around k_q is identical under the condition of fixed laser parameters, independently of the target, whereas the shift of k_q and the absolute yield of $P_c(k_z)$ depend on the target.

For a fixed-space molecule, the factorization formula has the same form as Eq. (12), with additional dependence of the molecular orientation angles of β in $f_\beta(|u_f|, \pi)$ and $W_\beta(k_z)$ through $A_{0\beta}$ and $\Gamma_\beta(F(t))$, namely,

$$P_{c\beta}(k_z) = |f_\beta(|u_f|, \pi)|^2 W_\beta(k_z) \quad (14)$$

and

$$W_\beta(k_z) = |\text{Ai}[C(k_z - k_q)]|^2$$

$$\times \left| \frac{2}{S_r'''} \right|^{2/3} \frac{16\pi^3 \varkappa |G_{00}(\beta)|^2 W_{00}(F(t_i))}{(t_r - t_i)^3 |F(t_i)|^2}$$

$$\times \exp\left(-\int_{-\infty}^{t_i} \Gamma_\beta(F(t))dt\right), \quad (15)$$

where Eq. (3) is used within the WFAT. Thus, the PEMD from a fixed-space molecule also exhibits the characteristic distribution described by the Airy function due to the doubly degenerate singularity of the rescattering action, as expressed in Eq. (14).

F. Orientation-averaged PEMD from randomly oriented nonpolar molecules

In order to compare our theory with the experimental PEMD measured for randomly oriented molecules, we should average Eq. (14) over the orientation angles. The orientation-averaged PEMD $\bar{P}_c(k_z)$ can be written in the form

$$\bar{P}_c(k_z) = \frac{1}{4\pi} \int_0^{2\pi} \int_0^\pi P_{c\beta}(k_z) \sin\beta \, d\beta \, d\alpha$$

$$= \bar{\sigma} \bar{W}(k_z), \quad (16)$$

where

$$\bar{\sigma} = \int_0^\pi |G_{00}(\beta) f_\beta(|u_f|, \pi)|^2$$

$$\times \exp\left(-\int_{-\infty}^{t_i} \Gamma_\beta(F(t))dt\right) \sin\beta \, d\beta \quad (17)$$
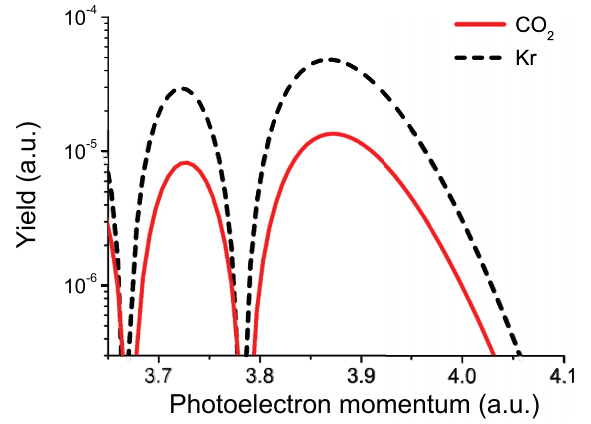

FIG. 2. PEMDs calculated around the outermost caustic of Kr (black dashed curve) and randomly oriented CO_2 (red solid curve) for pulses defined by Eq. (1) with a wavelength of 1600 nm, amplitude $F_0 = 0.0492$ a.u., and duration $T = 14$ fs at a CEP of zero using Eqs. (12) and (16).

represents the orientation-averaged DCS weighted with the structure factor and

$$\bar{W}(k_z) = |\text{Ai}[C(k_z - k_q)]|^2 \left| \frac{2}{S_r'''} \right|^{2/3}$$

$$\times \frac{8\pi^3 \varkappa W_{00}(F(t_i))}{(t_r - t_i)^3 |F(t_i)|^2} \quad (18)$$

is the orientation-averaged RWP. In this definition, the structure factor $G_{00}(\beta)$ and the depletion factor $\exp[-\int_{-\infty}^{t_i} \Gamma_\beta(F(t))dt]$ are separated from the RWP and incorporated into the DCS. As the Stark shift for a nonpolar molecule is small for the present laser parameters, the β dependence of the quantum shift is negligible as shown in Eq. (8). In this case, the k_z dependence described by the Airy function remains the same as those for atoms and fixed-space molecules.

Figure 2 shows $P_c(k_z)$ in Eq. (12) for Kr and $\bar{P}_c(k_z)$ in Eq. (16) for randomly oriented CO_2 for the outermost caustic at the wavelength of 1600 nm, amplitude $F_0 = 0.0492$ a.u., and duration $T = 14.0$ fs at the CEP ϕ of zero. As discussed, these targets exhibit almost the same E_0 of 14 eV and their Stark shifts are negligibly small. Evidently, both PEMDs exhibit almost identical relative shapes at the same position, described by the Airy function with almost the same argument. Notably, their absolute electron yields differ because of the target-dependent ionization rate and DCS. Here we also mention that the depletion factor is almost unity (greater than 0.99) and thus it is neglected in the following discussion.

III. EXPERIMENT

We measure the photoelectron momenta using a time-of-flight (TOF) spectrometer of 760 mm length. The experimental method and apparatus were described in Ref. [29]; only a brief outline is provided herein. The polarization direction of the ionizing pulses is set to the z axis, which is parallel to the TOF axis. The detection angle with respect to the TOF axis (z axis) is limited to approximately $1.5°$, corresponding to
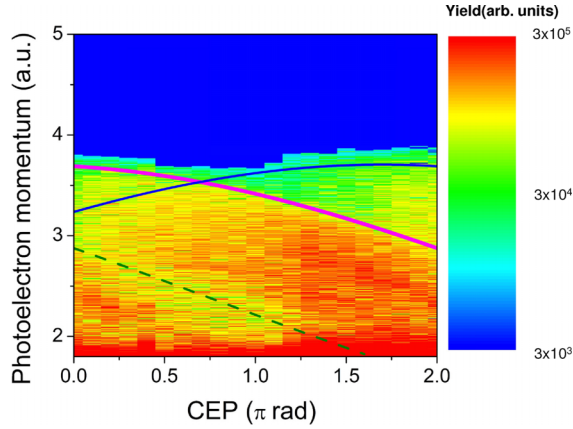
FIG. 3. PEMD of CO_2 measured as a function of the CEP ϕ at a pulse energy of 355 μJ. The three calculated caustic curves (thin blue solid, thick magenta solid, and thin green dashed) correspond to three different HCOs defined as HCO(−1), HCO(0), and HCO(1) at a peak field of $F_0 = 0.0460$ a.u. and pulse duration of 14 fs.

2×10^{-3} srad. The linearly polarized few-cycle infrared pulses at the center wavelength of 1600 nm are provided by an optical parametric chirped-pulse amplification system described in [49]. Thereafter, these pulses are focused into a target gas using a concave mirror with a focal length of 375 mm (f-number of approximately 75). In this experiment, the pulse is compressed to durations of approximately 14 fs. We use the targets of Kr and CO_2 gases, which have almost the same ionization potentials of 14 eV. The experimental conditions for the two gas targets are set almost identical to (i) confirm the target-independent coefficient C in the Airy function, which describes the PEMD around a caustic, and (ii) clarify the features of electron interferences based on multicenter rescattering and multiple scattering in the molecular case. The target gas is introduced into the TOF chamber with an effusive source. The CEP is controlled with an acousto-optic programmable dispersive filter (Fastlite, Dazzler HR45-1100-2200 T1). This method ensures the control of CEP without affecting the focusing condition and field envelope. The CEP is scanned in steps of 0.1π rad from 0 to 2π rad. In this study, we obtain a PEMD generated in tunnel ionization followed by rescattering, which is given in only one dimension along the k_z axis at $k_z > 0$.

The PEMDs of CO_2 measured as a function of CEP ϕ at a pulse energy of 355 μJ are illustrated in Fig. 3, which exhibits the CEP-dependent HCO structure in the PEMDs. At the fixed CEP, several caustics exist corresponding to the negative half cycles, which have already been discussed in a previous study [29]. In this study we define HCO(n) as the HCO generated by the half cycle of $F(t)$, which occupies the time interval $-3\pi/2 + 2n\pi < \omega t < -\pi/2 + 2n\pi$ (n is an integer number) at $\phi = 0$. The HCO(−1), HCO(0), and HCO(1) caustic curves calculated for the peak intensity $I = 7.4 \times 10^{13}$ W/cm^2 ($F_0 = 0.0460$ a.u.) and the pulse duration of 14 fs are plotted in Fig. 3.

To determine the peak intensity, pulse duration, and absolute CEP, we fit the measured PEMDs and their CEP dependences around the caustic to the calculated PEMDs originating from the tunneling in a specific half-cycle field

using a limited CEP range of $-0.3\pi \leqslant \phi \leqslant 0.7\pi$. The limited CEP range corresponds to the CEP range of $0 \leqslant \phi \leqslant 0.7\pi$ and $1.7\pi \leqslant \phi \leqslant 2.0\pi$ because of the 2π periodicity of PEMDs. The integration of the measured PEMDs in the entire momentum space is simply the total electron count, which corresponds to the relative probability. This indicates that the normalization factor of the measured PEMDs is an unknown parameter for determining the absolute ionization probability. The fitting procedure for determining the field parameters and the normalization factor of the measured photoelectron yields is described in Ref. [29].

IV. RESULTS AND DISCUSSION

The target-independent decay profile of a PEMD around an HCO is experimentally verified by comparing the results for Kr and CO_2. The results demonstrate that the momentum-dependent DCSs can be extracted from the CEP-dependent PEMDs around the HCOs. Furthermore, we observe that the electron interference by multicenter potential and the multiple scattering are imprinted in the PEMDs of CO_2 even in the case of randomly oriented ensembles.

A. Target-independent decay profile of a PEMD around an HCO

In this section we quantitatively compare the experimental and theoretical results. The measured PEMDs and those calculated using Eqs. (12) and (16) for Kr and randomly oriented CO_2, respectively, are displayed in Fig. 4 with CEPs ϕ of 0.0, 0.8π, and 1.6π at an estimated intensity I of 8.5×10^{13} W/cm^2 ($F_0 = 0.0492$ a.u.) and pulse durations of 14.1 and 14.0 fs. Using the estimated field parameters, we calculate three PEMDs from different half cycles of HCO(−1), HCO(0), and HCO(1), as depicted by blue, magenta, and green curves, respectively. The half cycles corresponding to three dominant HCOs are presented in the insets of Fig. 4. For HCO(0), the measured PEMDs beyond the quantum caustic are consistent with the theoretical results. Moreover, the existence of two other HCOs [HCO(−1) and HCO(1)] is consistent as well. Furthermore, as depicted in Figs. 4(c) and 4(f), the measured PEMDs agree with the calculations associated with HCO(−1) and HCO(0) in terms of their positions and relative yields.

As discussed in Sec. II, the PEMDs around a caustic calculated for Kr and randomly oriented CO_2 at the fixed laser parameters have the same relative distributions expressed by the squared Airy function. In Fig. 4 the PEMDs calculated for both targets are almost identical for similar laser parameters. To discuss the universal structure in the measured PEMDs around the caustic, the PEMDs of Kr and CO_2 at a CEP of 0.8π are normalized at the quantum caustics $k_q \sim 3.7$ a.u. to be equal to Ai$(0)^2 \simeq 0.126$, as shown in Fig. 5. Figure 5 clearly shows that the cutoff structures are identical and target independent. In addition, the squared Airy function (magenta dashed curve in Fig. 5) is consistent with the cutoff structure of the normalized PEMDs. These results are due to the fact that the coefficient C in Eq. (11) is independent of the target species and is determined using the laser parameters. The consistency between the calculated and measured PEMDs around
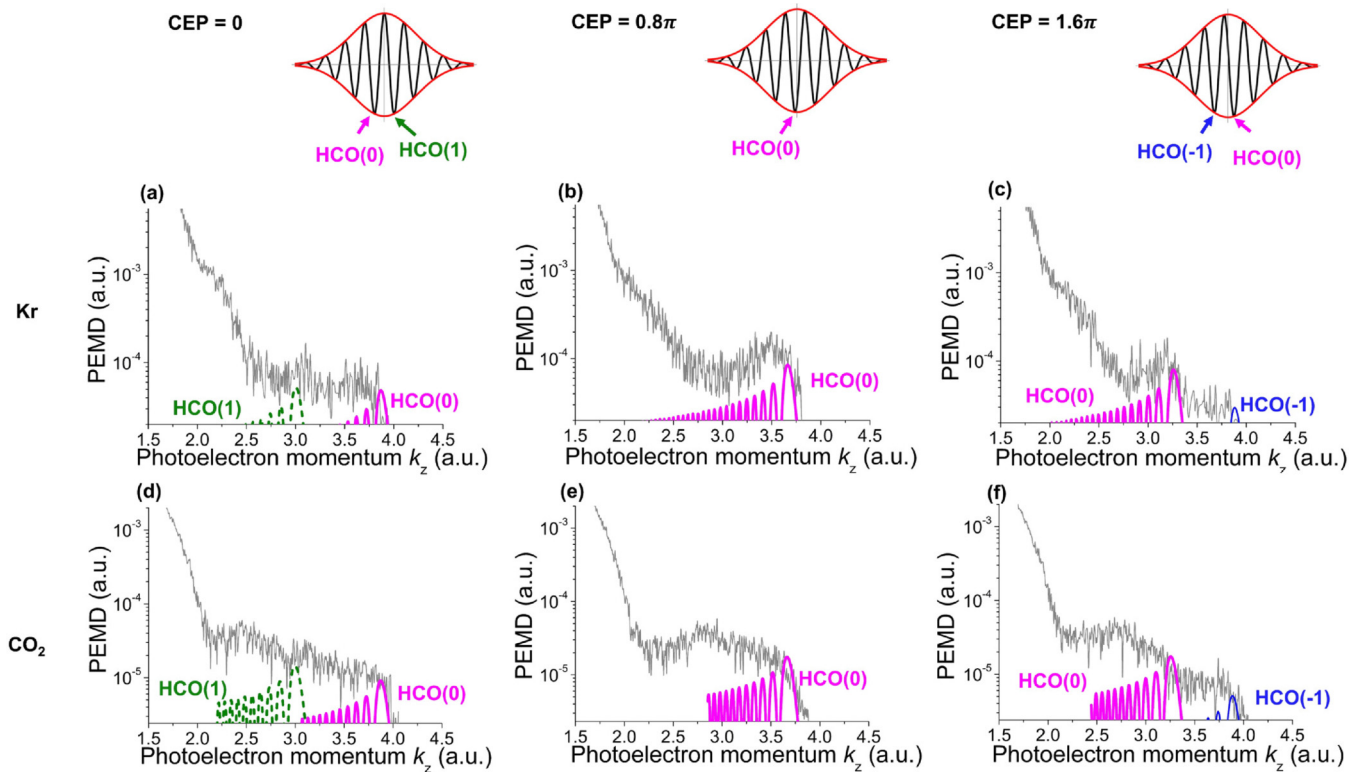
FIG. 4. PEMDs $P(k_z)$ of Kr and randomly oriented CO_2 (thin black curves) measured at selected CEPs ϕ of (a) and (d) 0, (b) and (e) 0.8π, and (c) and (f) 1.6π at an estimated effective intensity of 8.5×10^{13} W/cm^2 ($F_0 = 0.0492$ a.u.), and pulse durations of 14.1 and 14.0 fs. In the figures on top, thick magenta solid, thin blue solid, and thin green dashed curves show calculated PEMDs corresponding to a half cycle of the electric field. All calculated PEMDs are normalized using only one normalization factor N to match the measured PEMDs $P(k_z)$. Note that we set a common range on the vertical axis for a more comprehensive comparison, which makes the blue solid and green dashed curves progress out of the range in certain cases.

the caustic demonstrates the universal distribution described by the Airy function around the caustic due to the degenerate singularity of the action [31–33,36,37,50]. However, more
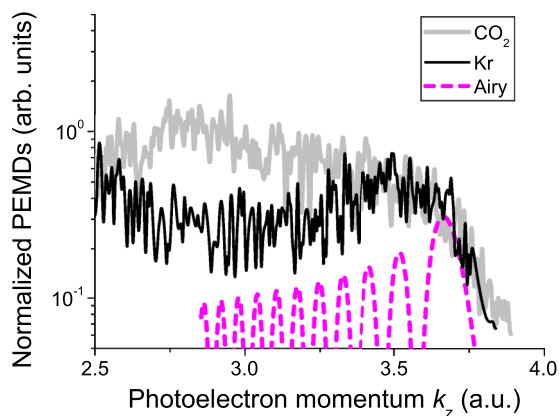

FIG. 5. Normalized PEMDs of Kr (thin black curve) and randomly oriented CO_2 (thick gray curve) at a CEP ϕ of 0.8π, which are identical to the black curves shown in Figs. 4(b) and 4(e), but these curves are normalized to Ai(0)$^2 \simeq 0.126$ at the quantum caustic. The calculated relative PEMDs (magenta dashed curve) is at an intensity of 8.5×10^{13} W/cm^2 ($F_0 = 0.0492$ a.u.) and a pulse duration of 14 fs, which is expressed by the squared Airy function. The position of the quantum caustic for the Airy function is located at that of a CO_2 molecule, and those of CO_2 and Kr are almost the same.

detailed discussions of the shape of the PEMDs are difficult in this study due to the low and noisy signals around the cutoff.

On the lower-energy side of the caustic, including the plateau region, certain discrepancies are observed between the measured and calculated PEMDs. Specifically, the PEMDs $P_c(k_z)$ calculated below the caustic show a continuous and gradually diminishing trend with oscillations, while the PEMDs $P(k_z)$ measured for CO_2 do not decline. Fundamentally, these findings are attributable to three reasons. As discussed in our previous study [29], the focal volume effect strongly affects a PEMD below the caustic and smears out the oscillating behavior. The second reason is the coherent sum of contributions from various half cycles in the PEMD, which appears below the caustic at the second-highest momenta. Third, the asymptotic form of the oscillatory integral, presenting the universal distribution described by the Airy function based on the singularity theory [31–33], is invalid in this region and holds only in a limited region, encompassing the classical and quantum caustics. In the plateau region located below the caustic, the two saddle points of action, corresponding to long and short trajectories, are almost independent. Thus, the usual-saddle-point method, the so-called semiclassical approximation, given in Eq. (A6) is adequate [10,51–53]. As observed in Fig. 4, a significant difference exists between the plateaus of the PEMDs measured for Kr and CO_2. The target dependence in the plateau region has

been reported in several theoretical [7,8,17] and experimental studies [20,23,25,27].

In addition, we measure the orientation-averaged PEMDs of CO_2, at estimated amplitudes of $F_0 = 0.0434$, 0.0460, and 0.0571 a.u. for pulse durations of 14.05, 14, and 13.85 fs, respectively. The above-mentioned characteristic distributions and features are also obtained, yielding the target-independent exponential decay of the orientation-averaged PEMDs of nonpolar molecules beyond the caustic.

B. Extraction of DCSs from CEP-dependent PEMDs beyond caustics

The laser parameters, elastic scattering DCSs, and tunneling ionization rate of a target are encoded in the PEMDs near HCOs. In this section we demonstrate the extraction of the momentum dependence of DCSs from the CEP-dependent PEMDs using the factorization formula. We follow the extraction scheme of the backscattering DCS, given in [29]. The first step involves the pulse characterization from the CEP-dependent PEMDs measured near HCOs by comparing the calculated PEMDs. The laser parameters are determined using the fitting procedure described in the Appendix of Ref. [29]. This procedure enables the accurate determination of the laser parameters (intensity, pulse duration, and absolute CEP), resulting in precise calculations of the position of the quantum caustic k_q. Subsequently, we divide the measured PEMD $P(k_z)$ by the calculated RWP $W(k_z)$ in Eq. (13) for Kr and $\bar{W}(k_z)$ in Eq. (18) for CO_2 with the estimated laser parameters. To avoid the errors caused by the volume effects, we use the exponentially decaying components of the PEMDs beyond the quantum caustics. To obtain an extracted DCS, we average $P(k_z)/W(k_z)$ or $P(k_z)/\bar{W}(k_z)$ over k_z above the quantum caustic k_q, because the corresponding DCS at the scattering momentum u_f is derived from the equation $P_c(k_z) = |f(|u_f|, \pi)|^2 W(k_z)$ for Kr or $\bar{P}_c(k_z) = \bar{\sigma} \bar{W}(k_z)$ for randomly oriented CO_2. Note that one data point of the extracted DCSs corresponds to the PEMD around the caustic at a specific CEP. Compared to the previous scheme [24], the proposed scheme yields more better statistics because it uses the PEMD $P(k_z)$ beyond the quantum caustic, not only the electron yield $P(k_z)$ at k_c. This extraction scheme of the DCS presumes that the calculated RWP is correct. Thus, we assume that the discrepancy between the measured and calculated PEMDs originates from an error related to the DCS. We use the PEMDs around HCO(0) only in the CEP range of $\phi = 0$ to 1.9π because the PEMDs around HCO(± 1) yield large errors due to poor statistics.

In Figs. 6 and 7 the extracted results for Kr^+ and CO_2^+ ions are compared with the DCSs obtained by solving the time-independent Schrödinger equation with the same SAE potentials used in the factorization formula. The extracted DCSs agree with the calculated DCSs, thereby confirming the extraction procedure for both atomic and molecular targets. In the case of CO_2 at an estimated field amplitude F_0 of 0.0571 a.u. and on the low-scattering-momentum side, corresponding to CEPs of 1.8π and 1.9π, we observe a certain discrepancy between the extracted and calculated DCSs. One of the primary reasons is distortion by the non-negligible contributions from the outer caustic HCO(-1). Notably, a similar
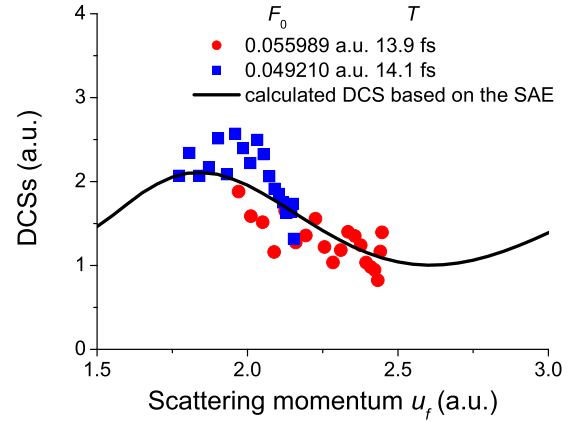

FIG. 6. Extracted DCSs $|f(|u_f|, \pi)|^2$ of Kr^+ for estimated field amplitudes F_0 of 0.0560 (circles) and 0.0492 a.u. (squares) with pulse durations T of 13.9 and 14.1 fs, respectively, as a function of the rescattering momentum u_f. The black curve represents DCSs $|f(|u_f|, \pi)|^2$ calculated by the SAE approximation.

discrepancy was observed in the Xe atom in our previous study [24]. Within the SAE approximation, the target dependence of the DCS is reflected by the effective one-electron potential or the effective charge of the parent ion. For the atomic targets, the effective charges determined from the experimental PEMDs are detailed in Refs. [20,38]. For the molecular targets, the interference effects from scattering by multicenter potential can be expected. Thus, we discuss the interference effects of three-center scattering of CO_2 in the following section.

C. Role of interference by multicenter rescattering in orientation-averaged DCSs of CO_2

In this section we discuss the interference effects of multicenter scattering in DCSs of CO_2^+. First, we consider the DCS $|f_\beta(|u_f|, \pi)|^2$ without the weight of the structure factor.
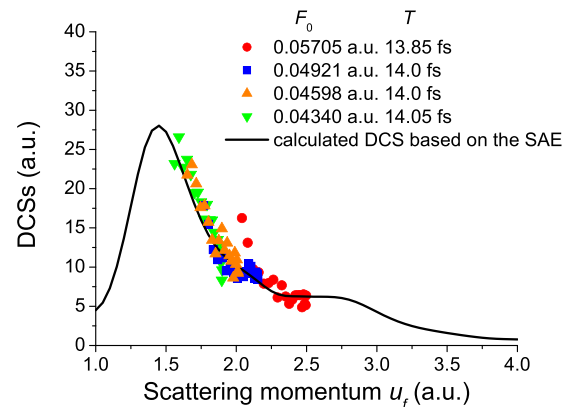

FIG. 7. Extracted orientation-averaged DCSs $\bar{\sigma}$ of CO_2^+ for estimated field amplitudes F_0 of 0.0571 (circles), 0.0492 (squares), 0.0460 (triangles), and 0.0434 a.u. (inverted triangles) with pulse durations T of 13.85, 14, 14, and 14.05 fs, respectively, as a function of the rescattering momentum u_f. The black curve represents orientation-averaged DCSs $\bar{\sigma}$ calculated by the SAE approximation, assuming that the depletion factor is unity.
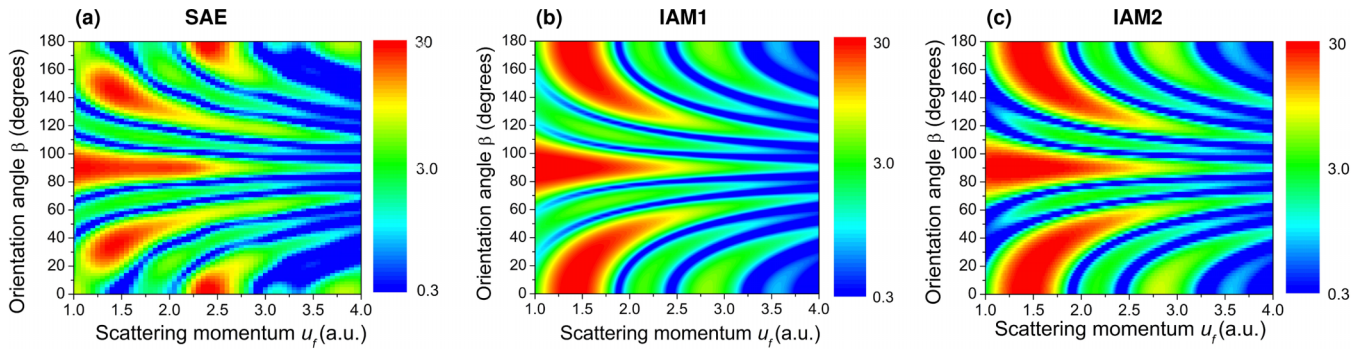
FIG. 8. Calculated DCSs $|f_\beta(|u_f|, \pi)|^2$ of CO_2^+ as a function of orientation angle β and scattering momentum u_f using (a) the SAE approximation, (b) the IAM with the ELSEPA code [54], and (c) the IAM with simple Yukawa potentials.

As is mentioned above, DCSs at $\theta = \pi$ are dependent on β and u_f, whereas they are independent of α. To deeply understand the backward elastic scattering process, we use three approaches to calculate the DCS for electron-ion elastic scattering: (i) SAE scattering calculations with the effective molecular potential implemented in Ref. [28], (ii) IAM calculations in which the scattering amplitude for a molecule is approximated by the sum of the scattering amplitudes of each atom, wherein the atomic scattering amplitudes are calculated using the program code ELSEPA [54], and (iii) IAM calculations approximating the atomic scattering amplitudes using the simple Yukawa screening potentials proposed by Xu *et al.* [40]. These approaches are referred to as SAE, IAM1, and IAM2 respectively. The calculated DCSs $|f_\beta(|u_f|, \pi)|^2$ are presented in Fig. 8 as a function of β and u_f. All calculations exhibit alternatively strong- and weak-interference stripe patterns. Within the IAM, the interference term between the ith and jth atoms with the same scattering amplitudes can be expressed as $\cos[2u_f R_{ij} \cos(\beta)]$ at $\theta = \pi$, where R_{ij} represents the interatomic distance. Based on the IAM interference term assuming the same scattering amplitudes for C and O, the strong stripes are identified as both constructive C-O and O-O interferences, whereas the weak ones come from only the constructive O-O interference. One can see clearly that the two IAM calculations are extremely similar, implying that a backward elastic scattering DCS is not sensitive to the atomic scattering amplitudes used in the calculations. We also see that the peak positions for the SAE approximation are slightly shifted from those for the IAM and the SAE result exhibits a richer structure than the IAM results. These are because the IAM considers only single-scattering events and neglect

multiple scattering, while the SAE approximation includes all multiple-scattering processes.

Furthermore, we observe the DCS with the weight of the structure factor $|G_{00}(\beta)|^2$, referring to the integrand in Eq. (17) and neglecting the depletion factor. The calculated results of the weighted DCSs of CO_2 are depicted in Fig. 9 as a function of β and u_f. As obtained, the rescattering processes at the molecular orientation in the vicinities of $\beta = 0°$ and $90°$ barely contribute to the orientation averaged DCSs, because of the nodal structure of $G_{00}(\beta)$ of CO_2, reflecting the π_g orbital. The rescattering process at the orientation angle of $\beta = 40°$ primarily contributes to the orientation-averaged DCSs. As indicated in Fig. 10, the interference effects persisted in the orientation-averaged DCSs. The fundamental peak at $u_f = 1.5$ a.u. can be assigned to the constructive C-O interference. In addition, the protuberance at $u_f = 2.8$ a.u is attributable to the constructive C-O interference. The O-O interference around $u_f = 2.0$ a.u forms a small shoulder structure in the orientation-averaged DCSs. Due to the tunneling ionization weight, these interference effects predominantly originate from the orientation angles between $10°$ and $40°$. Thus, we conclude that the momentum dependence of the orientation-averaged DCS continues to display the interference patterns. As noted from Fig. 10, the DCSs calculated by the two IAM calculations are not inconsistent with those obtained by the SAE. At a lower-scattering-momentum range less than 2.5 a.u., significant discrepancies are found between SAE and IAM calculations. As the IAM considers only single scattering by constituent atoms, the model calculation is valid only at a higher-momentum region. Overall, the SAE approximation is still valid in the scattering momentum range
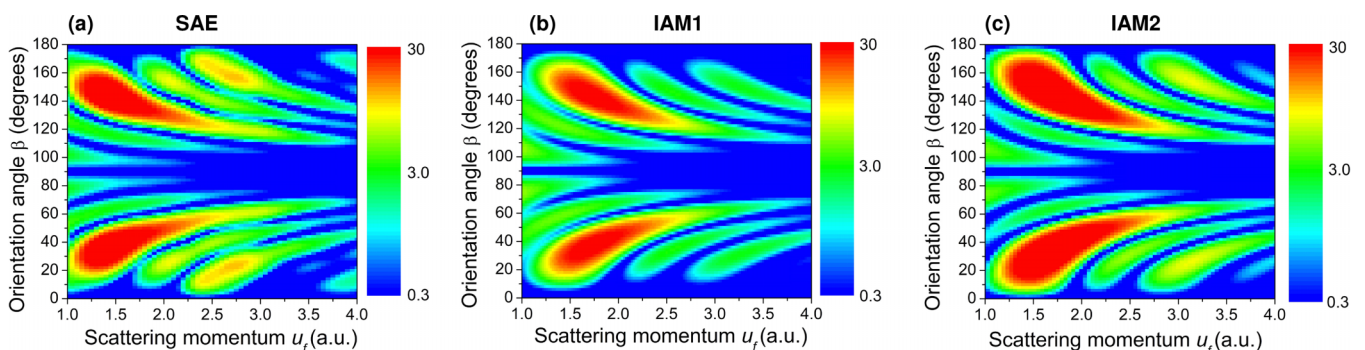

FIG. 9. Calculated DCSs $|G_{00}(\beta) f_\beta(|u_f|, \pi)|^2$ weighted by the structure factor of CO_2.
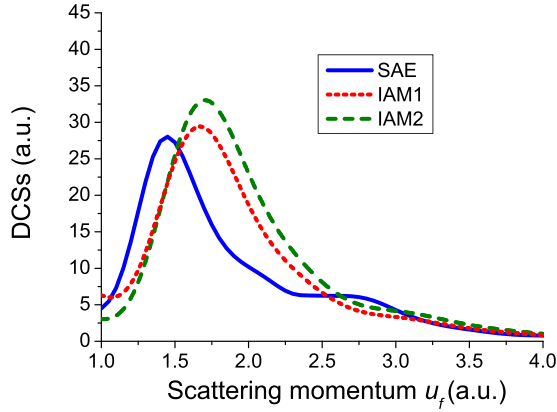
FIG. 10. Calculated orientation-averaged DCSs $\bar{\sigma}$ of $CO_2{}^+$. Blue solid curve represents the SAE approximation, which is identical to the black curve in Fig. 7. The red dotted curve and green dashed curve denote IAM1 and IAM2, respectively.

FIG. 11. Experimental and calculated MCFs of $CO_2{}^+$. The blue solid curve represents the SAE approximation, whereas the red dotted and green dashed curves represent IAM1 and IAM2, respectively. Symbols represent experimental MCFs from the extracted cross sections, similar to that in Fig. 7.

between 1.5 and 2.5 a.u. and it accurately reproduces the extracted DCSs, as depicted in Fig. 7. Therefore, we suggest that the adiabatic theory and SAE approximation can accurately analyze the DCSs, including the structure information in the lower-scattering-momentum region, where the IAM fails to yield accurate results due to the lack of multiple scattering [40]. Notably that there is a shape resonance at $u_f \sim 1.3$ a.u. [22], which is not discussed herein.

To quantitatively discuss the interference effects, we introduce a molecular contrast factor (MCF) $\mathcal{F}$, given as

$$\mathcal{F} = \frac{\bar{\sigma} - \int |G_{00}(\beta)|^2 \sigma_A \sin\beta \, d\beta}{\int |G_{00}(\beta)|^2 \sigma_A \sin\beta \, d\beta}, \quad (19)$$

where $\sigma_A = \sum_i |f_i|^2$ and f_i represents the atomic scattering amplitude of the atom labeled by i. Here σ_A is an incoherent sum of the scattering cross sections from all the atoms in the molecule. To determine the experimental MCFs based on the extracted DCSs and those calculated by the SAE approximation, we use the calculated σ_A by the ELSEPA code [54], which is identical to the NIST database [55]. Within the IAM, the MCF can be expressed as

$$\mathcal{F} = \frac{\sum_{i \neq j} \int |G_{00}(\beta)|^2 f_i f_j e^{i2u_f \cos(\beta) \cdot R_{ij}} \sin\beta \, d\beta}{\int |G_{00}(\beta)|^2 \sigma_A \sin\beta \, d\beta}. \quad (20)$$

The MCF shows an oscillatory behavior due to the interference term.

The experimental and calculated MCFs are illustrated in Fig. 11. The SAE calculations are in good agreement with the measured MCFs. Specifically, two points of the experimental MCFs at an estimated field amplitude $F = 0.0571$ a.u. and CEPs of 1.8π and 1.9π vary from the SAE calculations, similar to the DCS results. All MCFs predominantly exhibit an oscillatory behavior, corresponding to the molecular bond lengths. The experimental MCFs and those calculated by the SAE clearly show constructive interference by the C-O scattering at $u_f = 1.5$ and 2.8 a.u. Since the O-O bond length is twice that of the C-O bond, a weak oscillatory component with twice the frequency of C-O scattering is superimposed, resulting in a slight enhancement of the large peaks at 1.5
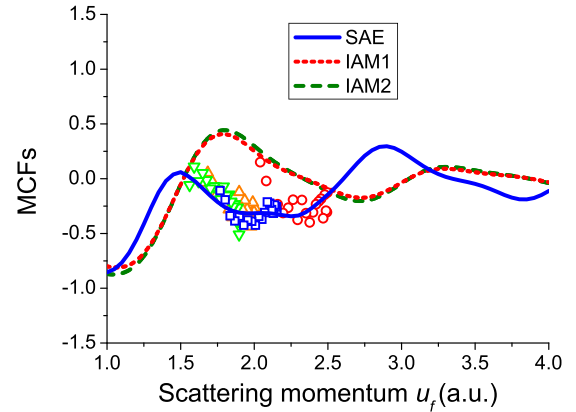
and 2.8 a.u. and the appearance of small peaks at $u_f = 2.2$ and 3.5 a.u. Although the MCFs calculated by the two IAMs show a similar behavior, they completely differ from the experimental MCFs even in the high-momentum range up to 2.5 a.u. The phases of the oscillations of the MCFs calculated by the IAMs vary from the experimental and calculated MCFs by the SAE approximation, while the frequencies of the interference patterns are almost identical for all MCFs. These features highlight that the multiple-scattering processes are non-negligible in the molecular rescattering in the measured momentum range. Overall, the present findings demonstrate that the SAE approximation can be used to determine the molecular structures from the extracted DCSs in the low-momentum ranges, where IAMs are invalid.

V. CONCLUSION

We experimentally and theoretically explored the rescattering PEMDs at the polarization direction for Kr atoms and randomly oriented CO_2 molecules near HCOs using the CEP-stable few-cycle infrared pulses. The cutoff structure of the PEMDs is associated with a caustic, corresponding to the doubly degenerate saddle point of the action. The adiabatic theory predicted that the shape of the PEMDs around the caustics is determined using only the laser pulse, which was confirmed by comparing the decay profile of the normalized PEMDs beyond the quantum caustic for Kr and CO_2 at fixed laser parameters. The CEP-dependent PEMDs displayed the target dependence originated from the target-dependent DCSs and tunneling ionization rates. Based on the factorization formula expressed by the product of the DCS and RWP, we extracted the DCSs from the measured PEMDs beyond the caustics using calculated RWPs. For both Kr and CO_2, the extracted DCSs agree with those calculated by the SAE approximation. We also found that the extracted DCSs of CO_2 do not agree with the IAM, as it considers only the single-scattering processes. The orientation-averaged DCSs of CO_2 still exhibited the interference signal scattered by the multicenter potential. Although the experimental MCFs are

also in good agreement with the SAE, the MCFs between the SAE approximation and the IAM vary completely up to 4 a.u. of the incident electron momentum. This indicates that the multiple scattering in molecules is non-negligible in the present momentum range of 1.5–2.5 a.u. Conclusively, the adiabatic theory and SAE approximation also hold for lower scattering momentum. Moreover, these theoretical and calculation methods are highly beneficial in analyzing the molecular structure using the rescattering processes, even in randomly oriented molecules. The CEP mapping method [24,29] combined with the adiabatic theory [10,13] enables the extraction of the well-defined elastic scattering processes for atoms as well as randomly oriented molecules from rescattered PEMDs beyond caustics.

ACKNOWLEDGMENTS

APPENDIX A: DEGENERATE SINGULARITY AND ITS UNIVERSALITY IN THE HAMILTONIAN FORMULATION

The basic concepts of the singularity theory are briefly introduced herein [31–37]. In particular, we provide a short description of a well-known type of simple degenerate singularity in an action, referred to as the caustic in optics [56,57], classical [58] and quantum mechanics [50,59], and catastrophe theory [60]. In principle, the singularity theory can provide the classification [31–33] and explain the stability [36,37] of a caustic. Moreover, it is guaranteed that the universal asymptotic form of oscillatory integrals around a caustic appears [31,33,50]. It usually emerges in Fourier transform and scattering amplitudes. The universal distribution of the oscillatory integrals around a caustic is characterized only by the class of a caustic [34,35].

1. General concept of degenerate singular points and caustics

Singularities of an action appear in various fields in optics [56,57], condensed-matter physics [59,61,62], scattering theory [50], and dynamical systems [58]. In particular, a caustic, which corresponds to a degenerate singularity of an action described by the Hamilton formulation [31–33], is one of the essential singularities. Interestingly, universal behaviors, such as rainbow arcs and cusp structures described by the Airy and Pearcey functions, appear around the caustic. The singularity theory can explain the underlying universality and scaling law of such a behavior and classify them using the equivalence class [31–33]. Notably, the caustics belonging to the same equivalence class can be transformed into the same normal form by diffeomorphic mapping in all cases [31–37,63].

Generally, the singular point t_0 of an action $S(t; \boldsymbol{k})$ is defined as

$$\partial S(t_0; \boldsymbol{k}_0)/\partial t = 0, \tag{A1}$$

where t denotes time and $\boldsymbol{k}$ represents parameters such as the final photoelectron momentum or the $\boldsymbol{k}$ vector of HHG. The singular point t_0 of $S(t; \boldsymbol{k})$ is called a saddle point or a critical point in physics. Thus, Eq. (A1) is also called the saddle-point equation. If the root is degenerate, it is called a degenerate singular point and the corresponding degenerate singular condition can be given by

$$\partial S(t_0; \boldsymbol{k}_0)/\partial t = \partial^2 S(t_0; \boldsymbol{k}_0)/\partial t^2 = 0. \tag{A2}$$

In this case, $\boldsymbol{k}_0$ is the caustic corresponding to the degenerate singularity. The degenerate singular point and caustic appear in many distinct phenomena such as quantum phase transitions [59], atomic collisions [50], and strong-field phenomena [6,11–13,29,64–74]. The simple degenerate singularities of an action described by the Hamiltonian formulation have been completely elucidated in mathematics [31–37]. The caustic is located at a position in which two or more classical trajectories or rays of light coalesce in $\boldsymbol{k}$ space. Thus, a caustic is a generalized concept of a focal point in optics and exhibits universal behaviors.

2. Classification of caustics

We assume that an action $S(t)$ is approximated as a polynomial. Notably, the polynomials are a subclass of the C^∞ functions and do not include the exponential function and trigonometric functions, which exhibit an infinite-order Taylor series. The analytic functions can be expanded by the infinite-order Taylor series, meaning that the polynomials can approximate the analytic functions with arbitrary accuracy. This assumption guarantees that the action can be Taylor expanded up to finite order. Moreover, in the case of a one-variable polynomial, it allows only the simple singularities that have already been classified in mathematics [31–35]. The singular points of the one-variable polynomial action can be classified as

$$\partial S(t_0)/\partial t = \partial^2 S(t_0)/\partial t^2 = \cdots = \partial^n S(t_0)/\partial t^n = 0,$$
$$\partial^{n+1} S(t_0)/\partial t^{n+1} \neq 0. \tag{A3}$$

This equation is equivalent to the condition that the saddle point of $S(t)$ is an n-degenerate root, which defines the A_n singularity. Furthermore, the A_n singular points are all in a one-variable polynomial $S(t)$. In contrast, a multivariable polynomial exhibits different classes of simple singularities such as D_n, E_n, $\ldots$ [31–37], which have been excluded from the scope of this research.

The degeneracy n completely characterizes the singularities of a one-variable polynomial action. From the Hamiltonian system perspective, the n-classical trajectories coalesce at the caustic associated with the A_n singularity. Notably, as the A_1 singular point is not degenerate, it is unrelated to a caustic and corresponds to only one classical trajectory.

The action $S(t; \boldsymbol{k})$ depends smoothly on the one-variable of time t as well as other parameters $\boldsymbol{k}$ (i.e., final emitted photoelectron momentum and $\boldsymbol{k}$ vector of HHG). The normal form of the action with the A_n singularity is defined in [31,32,34,35] and is given by

$$S_n(t; \boldsymbol{k}) = t^{n+1} + k_{n-1}t^{n-1} + k_{n-2}t^{n-2} + \cdots + k_2 t^2 + k_1 t, \tag{A4}$$

where the parameter $\boldsymbol{k}$ is an $(n-1)$-dimensional vector $(k_1, k_2, \ldots, k_{n-1})$. In all instances, an action around an A_n singular point can be transformed into the normal form by diffeomorphic mapping, meaning that the singularities are topologically invariant for diffeomorphic mapping. Thus, considering only the normal form is sufficient in the equivalent class of a caustic. When the dimension of parameter space $\boldsymbol{k}$ is m, the A_n singularity is stable under the condition of $n \leqslant m+1$ [31–33,36,37,63]. Thus, such a singularity is stable in a parameter space under small perturbations of the Hamiltonian and the initial wave front. In contrast, the higher-order A_n singularity ($n > m+1$) is unstable in an m-dimensional parameter space and the unstable singularities can be converted into the other class of singularity by small perturbations. Therefore, the universality of the singularity is guaranteed only for the stable singularity. Generally, in a finite-dimensional variable and parameter space, the stable singularities are limited to the finite equivalent classes [31–37]. For instance, in the case of a four-dimensional system, the stable classes of the caustics are limited to seven.

3. Asymptotic form of oscillatory integrals around the A_n singularity

The general form of oscillatory integrals [31,33], typically appearing in optics and scattering theory, can be expressed as

$$f(\boldsymbol{k}) = \int_{-\infty}^{\infty} g(t) \exp[iS(t;\boldsymbol{k})]dt, \tag{A5}$$

where a smooth function $S(t;\boldsymbol{k})$ denotes the action as a function of variable t and a set of parameters $\boldsymbol{k}$. Generally, $S(t;\boldsymbol{k})$ represents a phase of the electromagnetic fields in optics or the wave function in quantum mechanics and the function g denotes the amplitude. In addition, we assume that the action $S(t;\boldsymbol{k})$ is a complex function with a significantly small imaginary component. In case the part of $\exp[iS(t;\boldsymbol{k})]$ rapidly oscillates in comparison to $g(t)$, the saddle-point method can evaluate the integral [10,51–53]. In this approximation, the major contribution to the oscillatory integral arises from the saddle points (singular points), defined in Eq. (A1). The asymptotic form of the oscillatory integral is given as

$$f(\boldsymbol{k}) \sim \sum_{t_0} e^{i/4} \left(\frac{2\pi}{\partial^2 S(t_0;\boldsymbol{k})/\partial t^2} \right)^{1/2} g(t_0) \exp[iS(t_0;\boldsymbol{k})], \tag{A6}$$

where t_0 represents a set of the saddle points. The evaluation is performed by adding the contributions from all saddle points. In fact, this approximation is one of the most useful methods in strong-field physics [10,51–53]. However, it fails at the caustic and shows divergence due to the factor of $\partial^2 S(t_0;\boldsymbol{k})/\partial t^2 = 0$. The saddle-point method is valid at only the A_1 singularity and far from the caustic. Thus, an alternative approach is required to evaluate the oscillatory integral in the vicinity of the caustic.

Even at the caustic, the steepest-descent method is still valid if $\exp[iS(t;\boldsymbol{k})]$ rapidly oscillates compared with $g(t)$. Furthermore, $S(t;\boldsymbol{k})$ should be Taylor expanded around the A_n singular point up to $(n+1)$th order. As mentioned above, the action around the A_n singular point can always be transformed into the normal form $S_n(t;\boldsymbol{k})$ by diffeomorphic mapping;

thus, considering only the normal form $S_n(t;\boldsymbol{k})$ defined by Eq. (A4) is sufficient. The details of the method are reported in Refs. [31,33]; only the asymptotic form is presented as

$$f(\boldsymbol{k}) = \int_{-\infty}^{\infty} g(t) \exp[iS_n(t;\boldsymbol{k})]dt$$

$$\sim g(0) \int_{-\infty}^{\infty} \exp[iS_n(t;\boldsymbol{k})]dt$$

$$\sim g(0)\Phi_n(\boldsymbol{k}),$$

$$\Phi_n(\boldsymbol{k}) = \int_{-\infty}^{\infty} \exp[iS_n(t;\boldsymbol{k})]dt, \tag{A7}$$

where the caustic is located at the origin of $\boldsymbol{k} = 0$ and at $t = 0$ in the normal form. The primary contribution to the oscillatory integral is also from the vicinity of the caustic, because the caustic corresponds to the degenerate saddle point. The universal distribution $\Phi_n(\boldsymbol{k})$ is completely determined only by the class of singularity of the action $S(t;\boldsymbol{k})$. If the action has A_n singularity, the oscillatory integral around the caustic yields the universal distribution, which is deformed by diffeomorphic mapping. Moreover, the universal distributions associated with the A_2 and A_3 singularities exhibit the Airy function and Pearcey functions, respectively.

Around the cutoff region of HHG and a backward rescattered photoelectron momentum distribution, the A_2 singular point exists and the spectra exhibit the Airy functionlike universal distribution [6,11–13,29,64–67]. The same universal structures, such as the Airy and Pearcey functions, appear in various fields of optics [56,57], quenched spin chains [59], atomic collisions [50], and strong-field physics [6,11–13,29,64–73]. This universality originates from the topological invariant property of the caustic and is stable by small perturbations. In Ref. [74] a treatment of oscillatory integrals around the cutoff for the rescattering process was given.

APPENDIX B: AIRY FUNCTION AND PEARCEY FUNCTION AT THE A_2 AND A_3 SINGULARITIES

The Airy function $\text{Ai}(k)$ is related to the A_2 singularity and is defined as

$$\text{Ai}(k) \equiv \frac{1}{2\pi} \int_{-\infty}^{\infty} \exp[i(z^3/3 + kz)]dz = \frac{\sqrt[3]{3}}{2\pi} \Phi_2(\sqrt[3]{3}k). \tag{B1}$$

Therefore, the Airy function $\text{Ai}(k)$ is related to the universal function $\Phi_2(k)$, defined in Eq. (A7), i.e., the Airy function always appears around the A_2 singular point. Here we present a more practical form, assuming that a function $S(t, k)$ can be approximately Taylor expanded to third order around t_0, such as in

$$S(t, k) \simeq S(t_0, k) + S'(t_0, k)(t - t_0) + S''(t_0, k)(t - t_0)^2/2$$

$$+ S'''(t_0)(t - t_0)^3/6. \tag{B2}$$

Indeed, any third-order polynomials can be transformed into the form

$$S(t, k) \simeq S(\tilde{t}_0, k) + S'(\tilde{t}_0, k)[t - \tilde{t}_0(k)]$$

$$+ S'''(t_0)[t - \tilde{t}_0(k)]^3/6, \tag{B3}$$

where $\tilde{t}_0 = t_0 - S''(t_0, k)/S'''(t_0)$ and the term $(t - \tilde{t}_0)^2$ vanishes in Eq. (B3). Generally, $\tilde{t}_0$ is not a degenerate singular

point, but it becomes the doubly degenerate singular point of the action only if the action has the doubly degenerate singular point. This is based on the transformability of the action associated with the doubly degenerate singularity into the normal form [Eq. (A4)]. Without loss of generality, the asymptotic form of the oscillatory integral is presented around the A_2 singularity, given as

$$\int_{-\infty}^{\infty} \exp[iS(t)]dt = \exp[iS(\tilde{t}_0, k)] \left| \frac{2}{S'''(t_0)} \right|^{2/3}$$

$$\times \text{Ai}\left(S'(\tilde{t}_0, k) \left| \frac{2}{S'''(t_0)} \right|^{1/3} \right). \quad (B4)$$

Overall, this asymptotic form of the integrals is more practical, because the action of the considered system is usually derived as the Taylor expansion and not the normal form.

For the A_3 singularity, the Pearcey function $\text{Pe}(k_1, k_2)$ is related to $\Phi_3(k_1, k_2)$ and given as

$$\text{Pe}(k_1, k_2) \equiv \frac{1}{2\pi} \int_{-\infty}^{\infty} \exp[i(z^4/4 + k_2 z^2/2 + k_1 z)]dz. \quad (B5)$$

Therefore, the Pearcey function represents the universal distribution around the A_3 singularity.

[1] P. B. Corkum, Plasma Perspective on Strong Field Multiphoton Ionization, Phys. Rev. Lett. **71**, 1994 (1993).

[2] P. B. Corkum and F. Krausz, Attosecond science, Nat. Phys. **3**, 381 (2007).

[3] M. Meckel, D. Comtois, D. Zeidler, A. Staudte, D. Pavičić, H. C. Bandulet, H. Pépin, J. C. Kieffer, R. Dörner, D. M. Villeneuve, and P. B. Corkum, Laser-induced electron tunneling and diffraction, Science **320**, 1478 (2008).

[4] G. G. Paulus, W. Becker, W. Nicklich, and H. Walther, Rescattering effects in above-threshold ionization: A classical model, J. Phys. B **27**, L703 (1994).

[5] T. Morishita, A.-T. Le, Z. Chen, and C. D. Lin, Accurate Retrieval of Structural Information from Laser-Induced Photoelectron and High-Order Harmonic Spectra by Few-Cycle Laser Pulses, Phys. Rev. Lett. **100**, 013903 (2008).

[6] M. V. Frolov, N. L. Manakov, and A. F. Starace, Analytic formulas for above-threshold ionization or detachment plateau spectra, Phys. Rev. A **79**, 033406 (2009).

[7] Z. Chen, A.-T. Le, T. Morishita, and C. D. Lin, Quantitative rescattering theory for laser-induced high-energy plateau photoelectron spectra, Phys. Rev. A **79**, 033409 (2009).

[8] A. Čerkić, E. Hasović, D. B. Milošević, and W. Becker, High-order above-threshold ionization beyond the first-order Born approximation, Phys. Rev. A **79**, 033413 (2009).

[9] O. I. Tolstikhin, T. Morishita, and S. Watanabe, Adiabatic theory of ionization of atoms by intense laser pulses: One-dimensional zero-range-potential model, Phys. Rev. A **81**, 033415 (2010).

[10] O. I. Tolstikhin and T. Morishita, Adiabatic theory of ionization by intense laser pulses: Finite-range potentials, Phys. Rev. A **86**, 043417 (2012).

[11] M. V. Frolov, D. V. Knyazeva, N. L. Manakov, A. M. Popov, O. V. Tikhonova, E. A. Volkova, M.-H. Xu, L.-Y. Peng, L.-W. Pi, and A. F. Starace, Validity of Factorization of the High-Energy Photoelectron Yield in Above-Threshold Ionization of an Atom by a Short Laser Pulse, Phys. Rev. Lett. **108**, 213002 (2012).

[12] M. V. Frolov, D. V. Knyazeva, N. L. Manakov, J.-W. Geng, L.-Y. Peng, and A. F. Starace, Analytic model for the description of above-threshold ionization by an intense short laser pulse, Phys. Rev. A **89**, 063419 (2014).

[13] T. Morishita and O. I. Tolstikhin, Adiabatic theory of strong-field photoelectron momentum distributions near a backward rescattering caustic, Phys. Rev. A **96**, 053416 (2017).

[14] M. Okunishi, T. Morishita, G. Prümper, K. Shimada, C. D. Lin, S. Watanabe, and K. Ueda, Experimental Retrieval of Target Structure Information from Laser-Induced Rescattered Photoelectron Momentum Distributions, Phys. Rev. Lett. **100**, 143001 (2008).

[15] D. Ray, B. Ulrich, I. Bocharova, C. Maharjan, P. Ranitovic, B. Gramkow, M. Magrakvelidze, S. De, I. V. Litvinyuk, A. T. Le, T. Morishita, C. D. Lin, G. G. Paulus, and C. L. Cocke, Large-Angle Electron Diffraction Structure in Laser-Induced Rescattering from Rare Gases, Phys. Rev. Lett. **100**, 143002 (2008).

[16] S. Micheau, Z. Chen, A. T. Le, J. Rauschenberger, M. F. Kling, and C. D. Lin, Accurate Retrieval of Target Structures and Laser Parameters of Few-Cycle Pulses from Photoelectron Momentum Spectra, Phys. Rev. Lett. **102**, 073001 (2009).

[17] D. B. Milošević, W. Becker, M. Okunishi, G. Prümper, K. Shimada, and K. Ueda, Strong-field electron spectra of rare-gas atoms in the rescattering regime: Enhanced spectral regions and a simulation of the experiment, J. Phys. B **43**, 015401 (2010).

[18] M. Okunishi, H. Niikura, R. R. Lucchese, T. Morishita, and K. Ueda, Extracting Electron-Ion Differential Scattering Cross Sections for Partially Aligned Molecules by Laser-Induced Rescattering Photoelectron Spectroscopy, Phys. Rev. Lett. **106**, 063001 (2011).

[19] C. I. Blaga, J. Xu, A. D. DiChiara, E. Sistrunk, K. Zhang, P. Agostini, T. A. Miller, L. F. DiMauro, and C. D. Lin, Imaging ultrafast molecular dynamics with laser-induced electron diffraction, Nature (London) **483**, 194 (2012).

[20] J. Xu, C. I. Blaga, A. D. DiChiara, E. Sistrunk, K. Zhang, Z. Chen, A.-T. Le, T. Morishita, C. D. Lin, P. Agostini, and L. F. DiMauro, Laser-Induced Electron Diffraction for Probing Rare Gas Atoms, Phys. Rev. Lett. **109**, 233002 (2012).

[21] C. Wang, M. Okunishi, R. R. Lucchese, T. Morishita, O. I. Tolstikhin, L. B. Madsen, K. Shimada, D. Ding, and K. Ueda, Extraction of electron-ion differential scattering cross sections for C_2H_4 by laser-induced rescattering photoelectron spectroscopy, J. Phys. B **45**, 131001 (2012).

[22] M. Okunishi, R. Lucchese, T. Morishita, and K. Ueda, Rescattering photoelectron spectroscopy of small molecules, J. Electron Spectrosc. Relat. Phenom. **195**, 313 (2014).

[23] B. Wolter, M. G. Pullen, M. Baudisch, M. Sclafani, M. Hemmer, A. Senftleben, C. D. Schröter, J. Ullrich, R. Moshammer, and J. Biegert, Strong-Field Physics with Mid-IR Fields, Phys. Rev. X **5**, 021034 (2015).

[24] H. Geiseler, N. Ishii, K. Kaneshima, F. Geier, T. Kanai, O. I. Tolstikhin, T. Morishita, and J. Itatani, Carrier-envelope phase mapping in laser-induced electron diffraction, Phys. Rev. A **94**, 033417 (2016).

[25] B. Wolter, M. G. Pullen, A.-T. Le, M. Baudisch, K. Doblhoff-Dier, A. Senftleben, M. Hemmer, C. D. Schröter, J. Ullrich, T. Pfeifer, R. Moshammer, S. Gräfe, O. Vendrell, C. D. Lin, and J. Biegert, Ultrafast electron diffraction imaging of bond breaking in di-ionized acetylene, Science **354**, 308 (2016).

[26] Y. Ito, M. Okunishi, T. Morishita, O. I. Tolstikhin, and K. Ueda, Rescattering photoelectron spectroscopy of heterodiatomic molecules with an analytical returning photoelectron wave packet, Phys. Rev. A **97**, 053411 (2018).

[27] K. Amini, M. Sclafani, T. Steinle, A.-T. Le, A. Sanchez, C. Müller, J. Steinmetzer, L. Yue, J. R. Martínez Saavedra, M. Hemmer, M. Lewenstein, R. Moshammer, T. Pfeifer, M. G. Pullen, J. Ullrich, B. Wolter, R. Moszynski, F. J. García de Abajo, C. D. Lin, S. Gräfe, and J. Biegert, Imaging the Renner-Teller effect using laser-induced electron diffraction, Proc. Natl. Acad. Sci. USA **116**, 8173 (2019).

[28] M. Okunishi, Y. Ito, V. Sharma, S. Aktar, K. Ueda, R. R. Lucchese, A. I. Dnestryan, O. I. Tolstikhin, S. Inoue, H. Matsui, and T. Morishita, Rescattering photoelectron spectroscopy of the CO_2 molecule: Progress towards experimental discrimination between theoretical target-structure models, Phys. Rev. A **100**, 053404 (2019).

[29] T. Mizuno, N. Ishii, T. Kanai, P. Rosenberger, D. Zietlow, M. F. Kling, O. I. Tolstikhin, T. Morishita, and J. Itatani, Observation of the quantum shift of a backward rescattering caustic by carrier-envelope phase mapping, Phys. Rev. A **103**, 043121 (2021).

[30] E. T. Karamatskos, G. Goldsztejn, S. Raabe, P. Stammer, T. Mullins, A. Trabattoni, R. R. Johansen, H. Stapelfeldt, S. Trippel, M. J. J. Vrakking, J. Küpper, and A. Rouzée, Atomic-resolution imaging of carbonyl sulfide by laser-induced electron diffraction, J. Chem. Phys. **150**, 244301 (2019).

[31] V. Arnold, *Singularites of Caustics and Wave* (Springer, Dordrecht, 1990).

[32] V. Arnold, S. M. Gusein-Zade, and A. N. Varchenko, *Singularities of Differentiable Maps* (Birkhäuser, Boston, 1980), Vol. 1.

[33] V. Arnold, S. M. Gusein-Zade, and A. N. Varchenko, *Singularities of Differentiable Maps* (Ref. [32]), Vol. 2.

[34] V. Arnold, Normal forms of functions in neighborhoods of degenerate critical points, Russ. Math. Surv. **29**, 10 (1974).

[35] V. Arnold, Local normal forms of functions, Invent. Math. **35**, 87 (1976).

[36] K. Jänich, Caustic and catastrophes, Math. Ann. **209**, 161 (1974).

[37] G. Wassermann, Stability of caustics, Math. Ann. **216**, 43 (1975).

[38] T. Morishita, T. Umegaki, S. Watanabe, and C. Lin, High-resolution spatial and temporal microscopy with intense-laser-induced rescattering electrons, J. Phys.: Conf. Ser. **194**, 012011 (2009).

[39] M. Okunishi, R. Itaya, K. Shimada, G. Prümper, K. Ueda, M. Busuladžić, A. Gazibegović-Busuladžić, D. B. Milošević, and W. Becker, Two-Source Double-Slit Interference in Angle-Resolved High-Energy Above-Threshold Ionization Spectra of Diatoms, Phys. Rev. Lett. **103**, 043001 (2009).

[40] J. Xu, Z. Chen, A.-T. Le, and C. D. Lin, Self-imaging of molecules from diffraction spectra by laser-induced rescattering electrons, Phys. Rev. A **82**, 033403 (2010).

[41] M. G. Pullen, B. Wolter, A.-T. Le, M. Baudisch, M. Sclafani, H. Pires, C. D. Schröter, J. Ullrich, R. Moshammer, T. Pfeifer, C. D. Lin, and J. Biegert, Influence of orbital symmetry on diffraction imaging with rescattering electron wave packets, Nat. Commun. **7**, 11922 (2016).

[42] J. Xu, C. I. Blaga, K. Zhang, Y. H. Lai, C. D. Lin, T. A. Miller, P. Agostini, and L. F. DiMauro, Diffraction using laser-driven broadband electron wave packets, Nat. Commun. **5**, 4635 (2014).

[43] B. Belsa, K. Amini, X. Liu, A. Sanchez, T. Steinle, J. Steinmetzer, A. T. Le, R. Moshammer, T. Pfeifer, J. Ullrich, R. Moszynski, C. D. Lin, S. Gräfe, and J. Biegert, Laser-induced electron diffraction of the ultrafast umbrella motion in ammonia, Struct. Dyn. **8**, 014301 (2021).

[44] S.-J. Wang, J. Daněk, C. Blaga, L. F. DiMauro, J. Biegert, and C. D. Lin, Two-dimensional retrieval methods for ultrafast imaging of molecular structure using laser-induced electron diffraction, J. Chem. Phys. **155**, 164104 (2021).

[45] P. A. Batishchev, O. I. Tolstikhin, and T. Morishita, Atomic Siegert states in an electric field: Transverse momentum distribution of the ionized electrons, Phys. Rev. A **82**, 023416 (2010).

[46] O. I. Tolstikhin, T. Morishita, and L. B. Madsen, Theory of tunneling ionization of molecules: Weak-field asymptotics including dipole effects, Phys. Rev. A **84**, 053423 (2011).

[47] L. B. Madsen, O. I. Tolstikhin, and T. Morishita, Application of the weak-field asymptotic theory to the analysis of tunneling ionization of linear molecules, Phys. Rev. A **85**, 053404 (2012).

[48] L. D. Landau and E. M. Lifshitz, *Quantum Mechanics, Non-Relativistic Theory* (Pergamon, Oxford, 1977).

[49] N. Ishii, K. Kaneshima, K. Kitano, T. Kanai, S. Watanabe, and J. Itatani, Sub-two-cycle, carrier-envelope phase-stable, intense optical pulses at 1.6 μm from a BiB_3O_6 optical parametric chirped-pulse amplifier, Opt. Lett. **37**, 4182 (2012).

[50] J. N. L. Connor, Catastrophes and molecular collisions, Mol. Phys. **31**, 33 (1976).

[51] P. Salières, B. Carré, L. Le Déroff, F. Grasbon, G. G. Paulus, H. Walther, R. Kopold, W. Becker, D. B. Milošević, A. Sanpera, and M. Lewenstein, Feynman's path-integral approach for intense-laser-atom interactions, Science **292**, 902 (2001).

[52] A. Nayak, M. Dumergue, S. Kühn, S. Mondal, T. Csizmadia, N. Harshitha, M. Füle, M. Upadhyay Kahaly, B. Farkas, B. Major, V. Szaszkó-Bogár, P. Földi, S. Majorosi, N. Tsatrafyllis, E. Skantzakis, L. Neoričić, M. Shirozhan, G. Vampa, K. Varjú, P. Tzallas *et al.*, Saddle point approaches in strong field physics and generation of attosecond pulses, Phys. Rep. **833**, 1 (2019).

[53] A. Jašarević, E. Hasović, R. Kopold, W. Becker, and Milošević, Application of the saddle-point method to strong-laser-field ionization, J. Phys. A: Math. Theor. **53**, 125201 (2020).

[54] F. Salvat, A. Jablonski, and C. J. Powell, ELSEPA—Dirac partial-wave calculation of elastic scattering of electrons and positrons by atoms, positive ions and molecules, Comput. Phys. Commun. **165**, 157 (2005).

[55] NIST, Nist electron elastic-scattering cross-section database, https://srdata.nist.gov/srd64/.

[56] M. V. Berry and C. Upstill, Catastrophe optics: Morphoologies of caustics and their diffraction patterns, Prog. Opt. **18**, 257 (1980).

[57] M. V. Berry, Focusing and twinkling: Critical exponents from catastrophes in non-Gaussian random short waves, J. Phys. A: Math. Gen. **10**, 2061 (1977).

[58] V. I. Arnold, *Mathematical Methods of Classical Mechanics* (Springer, New York, 1978).

[59] W. Kirkby, J. Mumford, and D. H. J. O'Dell, Quantum caustics and the hierarchy of light cones in quenched spin chains, Phys. Rev. Res. **1**, 033135 (2019).

[60] R. Thom, *Structural Stability and Morphogenesis: An Outline of a General Theory of Models* (CRC, New York, 1989).

[61] A. Chandrasekaran, A. Shtyk, J. J. Betouras, and C. Chamon, Catastrophe theory classification of Fermi surface topological transitions in two dimensions, Phys. Rev. Res. **2**, 013355 (2020).

[62] N. F. Q. Yuan and L. Fu, Classification of critical points in energy bands based on topology, scaling, and symmetry, Phys. Rev. B **101**, 125120 (2020).

[63] R. Thom, *Structural Stability and Morphogenesis* (Benjamin, Reading, 1975).

[64] M. Lewenstein, P. Balcou, M. Y. Ivanov, A. L'Huillier, and P. B. Corkum, Theory of high-harmonic generation by low-frequency laser fields, Phys. Rev. A **49**, 2117 (1994).

[65] M. V. Frolov, N. L. Manakov, T. S. Sarantseva, and A. F. Starace, Analytic formulae for high harmonic generation, J. Phys. B **42**, 035601 (2009).

[66] Y. Okajima, O. I. Tolstikhin, and T. Morishita, Adiabatic theory of high-order harmonic generation: One-dimensional zero-range-potential model, Phys. Rev. A **85**, 063406 (2012).

[67] E. Pisanty, M. F. Ciappina, and M. Lewenstein, The imaginary part of the high-harmonic cutoff, J. Phys.: Photon. **2**, 034013 (2020).

[68] Y. Morimoto and P. Hommelhoff, Intracycle interference in the interaction of laser and electron beams, Phys. Rev. Res. **2**, 043089 (2020).

[69] O. Raz, O. Pedatzur, B. D. Bruner, and N. Dudovich, Spectral caustics in attosecond science, Nat. Photon. **6**, 170 (2012).

[70] D. Faccialà, S. Pabst, B. D. Bruner, A. G. Ciriolo, M. Negro, P. Prasannan Geetha, A. Pusala, N. Dudovich, S. Stagira, and C. Vozzi, High-order harmonic generation spectroscopy by recolliding electron caustics, J. Phys. B **51**, 134002 (2018).

[71] D. Faccialà, S. Pabst, B. D. Bruner, A. G. Ciriolo, S. De Silvestri, M. Devetta, M. Negro, H. Soifer, S. Stagira, N. Dudovich, and C. Vozzi, Probe of Multielectron Dynamics in Xenon by Caustics in High-Order Harmonic Generation, Phys. Rev. Lett. **117**, 093902 (2016).

[72] J. A. Uzan, G. Orenstein, A. Jiménez-Galán, C. McDonald, R. E. F. Silva, B. D. Bruner, N. D. Klimkin, V. Blanchet, T. Arusi-Parpar, M. Krüger, A. N. Rubtsov, O. Sminova, M. Ivanov, B. Yan, T. Brabec, and N. Dudovich, Attosecond spectral singularities in solid-state high-harmonic generation, Nat. Photon. **14**, 183 (2020).

[73] J. Chen, Q. Xia, and L. Fu, Reconstruction of crystal band structure by spectral caustics in high-order harmonic generation, Phys. Rev. A **104**, 063109 (2021).

[74] C. Figueira de Morisson Faria, H. Schomerus, and W. Becker, High-order above-threshold ionization: The uniform approximation and the effect of the binding potential, Phys. Rev. A **66**, 043413 (2002).